Journal of Alloys and Compounds 504 (2010) 314–319

Contents lists available at ScienceDirect

Journal of Alloys and Compounds

journal homepage: www.elsevier.com/locate/jallcom

Thermoelectric properties of $A_{0.05}Mo_3Sb_{5.4}Te_{1.6}$ (A = Mn, Fe, Co, Ni)

Hong Xu[a], Katja M. Kleinke[a], Tim Holgate[b], David Rossouw[c], Gianluigi Botton[c], Terry M. Tritt[b], H. Kleinke[a,*]

[a] Department of Chemistry, University of Waterloo, Waterloo, Ontario, Canada N2L 3G1
[b] Department of Physics and Astronomy, Clemson University, Clemson, SC 29634-0978, USA
[c] Materials Science and Engineering, McMaster University, Hamilton, Ontario, Canada L8S 4L7

ARTICLE INFO

Article history:
Received 13 May 2010
Received in revised form 25 May 2010
Accepted 25 May 2010
Available online 4 June 2010

Keywords:
Antimonide
Telluride
Electronic structure
Physical properties

ABSTRACT

$Mo_3Sb_{7-x}Te_x$ was earlier reported to be a promising *p*-type thermoelectric material for high temperature applications, with $Ni_{0.06}Mo_3Sb_{5.4}Te_{1.6}$ achieving a *ZT* of 0.93 at 1023 K. In order to investigate the effect of using different transition metal atoms and to further improve the thermoelectric properties, a variety of transition metal atoms (Mn, Fe, Co and Ni) were intercalated into the voids of empty Sb atom cubes. Our results indicate that $Fe_{0.05}Mo_3Sb_{5.4}Te_{1.6}$ and $Ni_{0.05}Mo_3Sb_{5.4}Te_{1.6}$ exhibit a higher power factor than $Mo_3Sb_{5.4}Te_{1.6}$. $Fe_{0.05}Mo_3Sb_{5.4}Te_{1.6}$ demonstrates the highest *ZT* value at 673 K (*ZT* = 0.31), significantly higher than $Mo_3Sb_{5.4}Te_{1.6}$. Thermal analysis proves $Ni_{0.05}Mo_3Sb_{5.4}Te_{1.6}$ to be phase stable at least until 1250 K in an inert atmosphere, an important prerequisite for high temperature applications.

1. Introduction

With the depletion of natural resources, the exploration of the alternative energy resources is becoming more and more imperative for sustainable development. Thermoelectric materials are attracting extensive interest because of their potential of converting temperature gradients into electricity [1]. Several automotive companies, such as General Motors, BMW, Ford and Toyota, are working on thermoelectric-based exhaust heat recovery to reduce the fuel consumption [2]. Moreover, thermoelectric materials are also employed as power supply in a variety of applications, such as radioactive thermoelectric generators (RTG) in spaceships (Voyager and Cassini) and for data gathering and telecommunication in remote terrestrial areas [3].

Thermoelectric materials are typically semiconductor with narrow band gaps, composed of heavy elements and comprising complicated crystal structures [4–7]. Thermoelectric materials are ranked by their dimensionless figure-of-merit, $ZT = TS^2\sigma/\kappa$, with *T* being the average absolute temperature between the hot and the cold side of the thermoelectric device. A high Seebeck coefficient (*S*), high electrical conductivity (σ) and low thermal conductivity (κ) are essential to achieve high *ZT* values. The thermoelectric efficiency depends on *ZT* and the temperature gradient via Eq. (1):

$$\eta = \frac{T_H - T_C}{T_H} \cdot \frac{\sqrt{1+ZT}-1}{\sqrt{1+ZT}+T_C/T_H} \quad (1)$$

The relatively low efficiency currently restricts wider applications of the thermoelectric energy conversion. Developing materials that can work at higher temperature (thus providing a higher temperature difference) with high *ZT* would significantly improve the thermoelectric efficiency. To date, the only commercial thermoelectric material for such high temperature applications is a solid solution of $Si_{1-x}Ge_x$. *n*-type $Si_{0.8}Ge_{0.2}$ exhibits a *ZT* of 1 around 1173 K, however the *p*-type $Si_{0.8}Ge_{0.2}$ only showed a *ZT* of 0.6 at similar temperature [8]. Other leading thermoelectric materials for high temperature applications include the *p*-type $Yb_{14}MnSb_{11}$ with *ZT* = 1.1 at 1275 K [9] and *n*-type $AgPb_{18}SbTe_{20}$ with *ZT* = 2.2 at 800 K [10].

About 10 years ago, the Kleinke group commenced to investigate the thermoelectric properties of $Mo_3Sb_{7-x}Te_x$ [11] and its variants with intercalated transition metal atoms [12–14]. Gascoin et al. showed in 2007 that $Mo_3Sb_{5.4}Te_{1.6}$ attains *ZT* = 0.80 at 1050 K [15], and in 2009, Candolfi et al. identified Mo_3Sb_7 as one of the best *p*-type thermoelectric metals with a *ZT* = 0.11 at 800 K [16]. They also reported on the magnetic and thermoelectric properties of $Mo_3Sb_{7-x}Te_x$ [17] and $Mo_{3-x}Ru_xSb_7$ [18,19]. Thus far, the highest *ZT* value achieved within this series of compounds is *ZT* = 0.93 at 1023 K, exhibited by $Ni_{0.06}Mo_3Sb_{5.4}Te_{1.6}$ [20]. In this paper, we examine the effect of using different transition metal atoms, i.e. Mn, Fe, and Co.

* Corresponding author.
E-mail address: kleinke@uwaterloo.ca (H. Kleinke).

0925-8388/$ – see front matter © 2010 Elsevier B.V. All rights reserved.
doi:10.1016/j.jallcom.2010.05.124

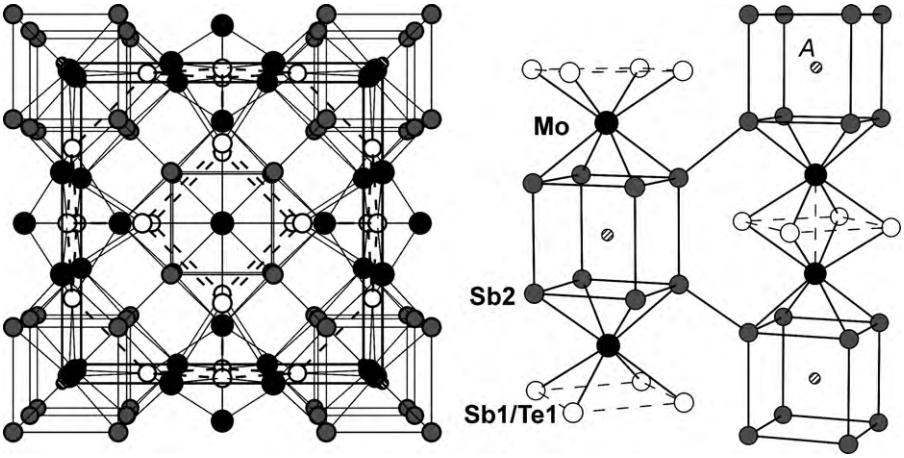

Fig. 1. Crystal structure of $A_xMo_3Sb_{7-x}Te_x$ (left) and fragments of its chains (right).

2. Experimental

2.1. Syntheses and analyses

All samples were prepared from the elements: molybdenum (powder, −100 mesh, 99.95%), antimony (powder, −100 mesh, 99.5%), tellurium (broken ingot, 99.99%), iron (powder, <10 μm, 99.9%) and nickel (powder, −200 mesh, 99.9%) were acquired from Alfa Aesar; manganese (powder, −50 mesh, 99.9%) and cobalt (powder, −100 mesh, 99.9%) were purchased from Aldrich. As shown in 2002/3 via single crystal structure determinations, less than 0.10 metal atoms (A = Mg, Fe, Co, and Ni) per formula unit can be added into the cubes of Sb2 atoms (there is only one cube for two formula units $Mo_3Sb_{7-x}Te_x$; completing filling would result in the formula of $A_{0.5}Mo_3Sb_{7-x}Te_x$) [12,20]. Therefore, an intermediate amount of 0.05 was chosen for all transition metal atoms. All the elements were weighed in the desired stoichiometric ratio, then mixed and loaded into silica tubes in the argon-filled glove box. These tubes were evacuated and sealed under vacuum, followed by heating in resistance furnaces at 993 K over a period of 10 days. The resulting products were thoroughly ground and analyzed via X-ray powder diffraction, utilizing INEL's powder diffractometer with a position sensitive detector. If any side product peaks were found, e.g. $MoTe_2$ or unreacted Sb, the samples were reloaded into new silica tubes to repeat the heating procedure. In most cases, these peaks disappeared during the second heating step. Only samples without any visible side products were sent to the Complex and Advanced Materials Laboratories (CAML) at Clemson University for the preparation of hot-pressed pellets and subsequent physical properties measurements on these pellets.

Differential scanning calorimetry (DSC) was used to investigate the thermal stability of Mo_3Sb_7 and $Ni_{0.05}Mo_3Sb_{5.4}Te_{1.6}$. The calorimetry experiment was performed between 300 K and 1473 K with computer controlled NETZSCH STA 409PC Luxx with a heating rate of 10 K/min. The samples were sealed in small silica ampoules under vacuum and placed into a flowing argon atmosphere for the measurement, as described before [21].

A hot-pressed pellet of the nominal composition $Ni_{0.05}Mo_3Sb_{5.4}Te_{1.6}$ was analyzed employing the LEO 1530 scanning electron microscope (SEM) with integrated EDAX Pegasus 1200, using an acceleration voltage of 20 kV. A part of this pellet was sent to McMaster University as well for high resolution transmission electron microscope (HRTEM) analysis on the Cs corrected FEI Titan TEM with a 300 keV acceleration voltage. TEM samples were prepared by low angle wedge tripod polishing. The thin tip of the wedge was ion milled at liquid nitrogen temperature to electron transparency.

2.2. Electronic structure calculations

The LMTO method (LMTO = linear muffin tin orbitals) with the atomic spheres approximation (ASA) [22,23] was utilized for the electronic structure calculations. The density functional theory with local density approximation (LDA) was employed to treat the exchange and correlation energies [24]. Although $A_{0.05}Mo_3Sb_{5.4}Te_{1.6}$ was the nominal composition investigated here, $Ni_{0.125}Mo_3Sb_{5.5}Te_{1.5}$ was depicted as a model in order not to use a too large unit cell. $Ni_{0.125}Mo_3Sb_{5.5}Te_{1.5}$ and $Mo_3Sb_{5.5}Te_{1.5}$ were calculated based on our crystallographic data obtained for Mo_3Sb_7 from the year 2002 [11], where half of the Sb1 atoms were substituted by Te atoms. The space group was thereby reduced from $Im\bar{3}m$ to $I4/mmm$, while retaining the unit cell size of Mo_3Sb_7 model. Next, we doubled the unit cell in order to fill only a quarter of the voids, necessitated by the 0.125 Ni per formula unit. The following wavefunctions were used: for Ni *4s*, *4p*, and *3d*; for Mo *5s*, *5p*, *4d* and *4f* included via the downfolding technique [25]; for Sb and Te *5s*, *5p*, and *5d*, *4f* (the last two downfolded). 256 *k* points of the first Brillouin zone were selected via an improved tetrahedron method [26].

2.3. Physical property measurements

Thermoelectric property measurements were carried out at CAML at Clemson University. All samples were hot-pressed under 175 MPa at 993 K for 1 h. The densities achieved were at least 96% of the theoretical maximum. Seebeck coefficient and electrical conductivity were determined at low temperature via a custom-built apparatus, with estimated errors of ±1 μV K^{-1} for the Seebeck coefficient and ±3% for the conductivity [27]. Subsequently, high temperature data were collected simultaneously on the ULVAC ZEM-2, and then scaled to match the 300 K data obtained from the custom-built apparatus. High temperature thermal conductivity data was calculated from the material density (ρ), thermal diffusivity (α) and specific heat (C_p) via the relationship of $\kappa = \rho\alpha C_p$. Thermal diffusivity was measured utilizing a laser flash system (NETZSCH LFA 457) with an estimated error of ±3%, and specific heat measurements were carried out on NETZSCH DSC system. These measurement setups were described previously [13,14].

3. Results and discussion

3.1. Crystal structure

The $Mo_3Sb_{7-x}Te_x$ crystallizes in the Ir_3Ge_7 structure type with the space group $Im\bar{3}m$. Because the structure of $Mo_3Sb_{7-x}Te_x$ was described in detail before [11], only a brief summary is given here. The transition metal atom A is located in the cube formed by eight Sb2 atoms. These Sb2 atoms are part of a square $Mo(Sb,Te)_8$ antiprism, and two such antiprisms share a face comprised of Sb1/Te1 (Fig. 1). The Sb2 atoms participate in intermediate Sb2–Sb2 bonds of 3.1 Å along the edges of the cube, and are also connected to the Sb2 atoms of the neighboring cubes via the shortest Sb2–Sb2 distance (2.9 Å). As we proposed in 2002, the Sb1 sites are partially occupied by Te1 atoms because Te has the higher electronegativity and prefers to occupy the site with less anion-anion bonding, such as the S atoms in ZrSiS [28] and CeAsS [29]. That supposition was confirmed via neutron diffraction by Candolfi et al. in 2008 [30]. A longer distance of 3.3 Å (dashed lines) occurs along the edges of the $(Sb1/Te1)_4$ square between the Mo atoms. All of these interactions contribute to the density of states, DOS, around the Fermi level [31]. In general, the chains of $Mo_3Sb_{7-x}Te_x$ are comprised of Sb2 cube–Mo–Sb1/Te1 square–Mo–Sb2 cube–Mo. . .. Three such chains penetrate each other at the Sb2 cubes to construct the three-dimensional structure. The transition metal atoms A = Mn, Fe, Co, Ni are intercalated into the Sb2 cubes to form eight A–Sb2 bonds of 2.6–2.7 Å [12].

3.2. Electron microscopy

The SEM map screens of the composing elements of $Ni_{0.05}Mo_3Sb_{5.4}Te_{1.6}$ are shown in Fig. 2. The distribution of Ni, Mo, Sb and Te appeared to be quite homogeneous throughout the sample.

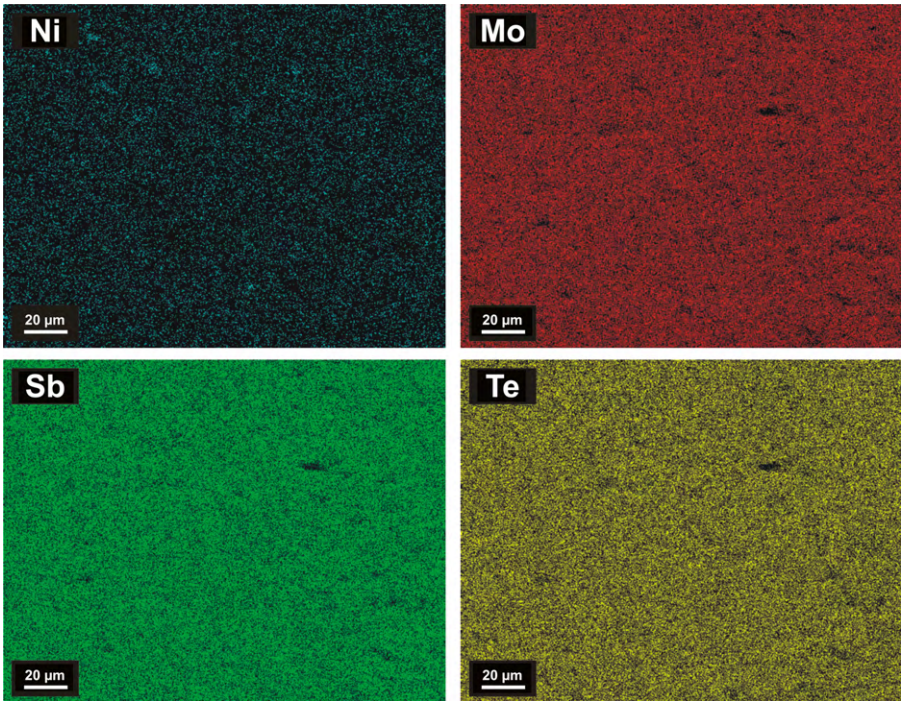

Fig. 2. SEM map screens of different elements of $Ni_{0.05}Mo_3Sb_{5.4}Te_{1.6}$.

Bright field TEM images show large single crystal regions in the sample (Fig. 3). Bend contours are apparent in thin regions where the crystal lattice is strained. The residual stain in the lattice is likely due to the mechanical thinning process. The SAED pattern is in good agreement with the one calculated [32] for the ⟨1 0 2⟩ zone axis orientation. The CBED pattern imaged down the same ⟨1 0 2⟩ zone axis displays $m\bar{3}m$ symmetry, consistent with the proposed space group $Im\bar{3}m$. Higher order Laue zones and Kikuchi lines are also visible in the CBED pattern and are in good agreement with the calculations. Finally, HRTEM phase contrast images reveal individual atomic columns in the lattice oriented down the ⟨1 0 2⟩ and ⟨1 0 1⟩ zone axis, indicating the high crystallinity of $Ni_{0.05}Mo_3Sb_{5.4}Te_{1.6}$. The somewhat mottled appearance in Fig. 3(g) is likely due to the presence of a thin amorphous layer on the surface of the sample. No nanostructured domains were detected.

3.3. Electronic structure

Our previous calculation showed $Mo_3Sb_5Te_2$ (with its 55 valence electrons) to be a semiconductor with a band gap of 0.6 eV [20]. As discussed previously [33], adding Ni will not significantly alter the valence electron concentration, as its *d* states

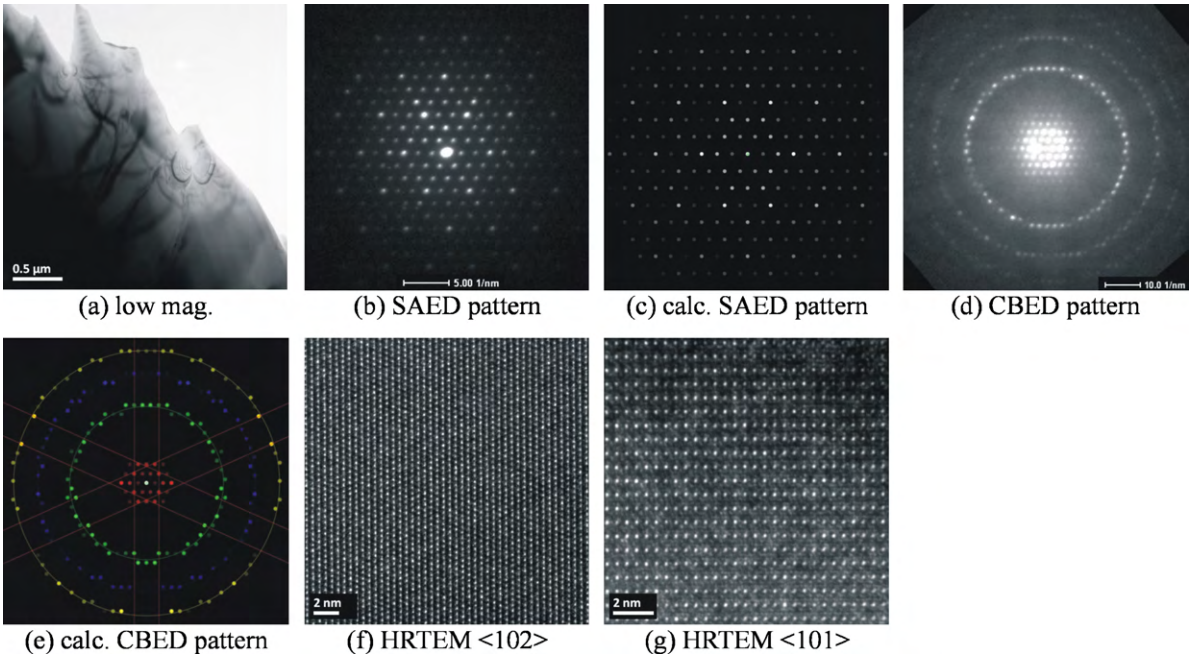

Fig. 3. TEM images of $Ni_{0.05}Mo_3Sb_{5.4}Te_{1.6}$.

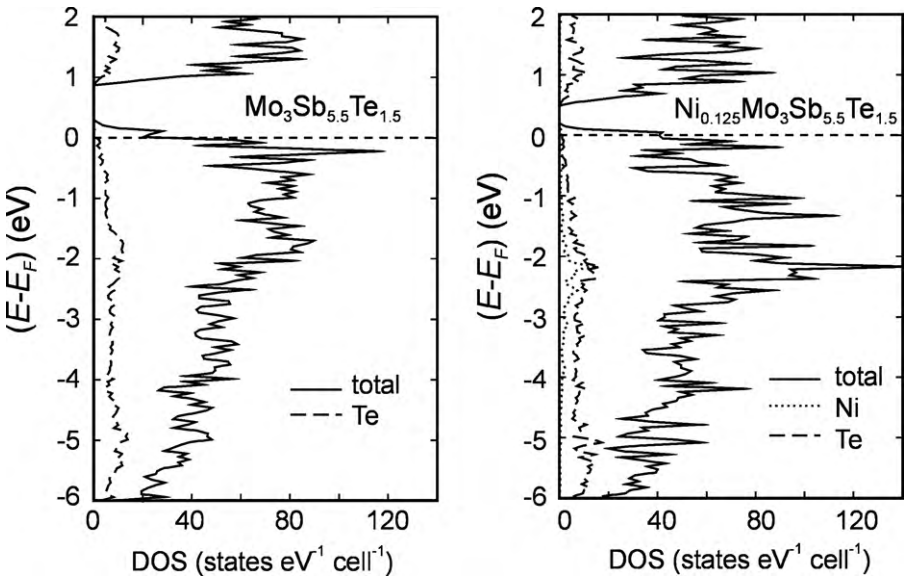

Fig. 4. Density of states of $Mo_3Sb_{5.5}Te_{1.5}$ (left) and $Ni_{0.125}Mo_3Sb_{5.5}Te_{1.5}$ (right).

were almost completely found below the Fermi level (E_F) in case of $Ni_{0.25}Mo_3Sb_5Te_2$. $Mo_3Sb_{5.5}Te_{1.5}$ with its fewer valence electrons is to be considered a *p*-doped semiconductor, where the top of the valence band is empty (left part of Fig. 4). By analogy, the same should be true for $Mo_3Sb_{5.4}Te_{1.6}$. Adding Ni to *p*-type $Mo_3Sb_{5.5}Te_{1.5}$ appears to reduce this material to some small extent, because some Ni *d* states are unfilled at the top of the valence band of $Ni_{0.125}Mo_3Sb_{5.5}Te_{1.5}$ (dotted line in the right part of Fig. 4). Also, the number of states at E_F appears to be slightly higher, but that may be an artifact of the calculation and the hypothetical character of the model with 0.125 Ni. In any case, Hall effect measurements yielded a higher charge carrier concentration of $Ni_{0.05}Mo_3Sb_{5.4}Te_{1.6}$, compared to $Mo_3Sb_{5.4}Te_{1.6}$ [13], which may be a consequence of the larger number of states at E_F.

Because of the high correlation in compounds with partially filled *3d* orbitals, the cases with, e.g. A = Mn and Fe cannot be reliably computed within the LMTO method. Nevertheless, the transition metal atom A in general contributes to the valence band, and changes the band gap size and number of states at E_F. For example, $Mo_3Sb_{5.5}Te_{1.5}$ has a band gap of 0.57 eV, and adding 0.125 Ni reduces the band gap to 0.30 eV. In conclusion, while a significant effect of using different transition metals A onto the physical properties is expected, it is hard to quantify.

3.4. Physical properties

All of our samples show reasonably high electrical conductivity values above $10^{+3}\,\Omega^{-1}\,cm^{-1}$ at 300 K. In each case, the electrical conductivity (σ) decreases with increasing temperature (Fig. 5), typical for a degenerate semiconductor, as the charge carrier concentration is basically independent of the temperature [13]. $Ni_{0.05}Mo_3Sb_{5.4}Te_{1.6}$ demonstrates the highest σ ($1800\,\Omega^{-1}\,cm^{-1}$ at 320 K), and $Co_{0.05}Mo_3Sb_{5.4}Te_{1.6}$ the lowest ($1500\,\Omega^{-1}\,cm^{-1}$ at 320 K). The difference of 20% is much higher than the estimated error of 3%. The sample without *3d* element (called "no A") exhibits the second highest σ ($1740\,\Omega^{-1}\,cm^{-1}$ at 320 K). $Mn_{0.05}Mo_3Sb_{5.4}Te_{1.6}$ and $Fe_{0.05}Mo_3Sb_{5.4}Te_{1.6}$ have virtually identical electrical conductivity values at 320 K, namely $1650\,\Omega^{-1}\,cm^{-1}$. With increasing temperature, σ of $Fe_{0.05}Mo_3Sb_{5.4}Te_{1.6}$ decreases slightly slower.

The Seebeck coefficient measurements confirmed that all title compounds are *p*-type semiconductors with Seebeck values

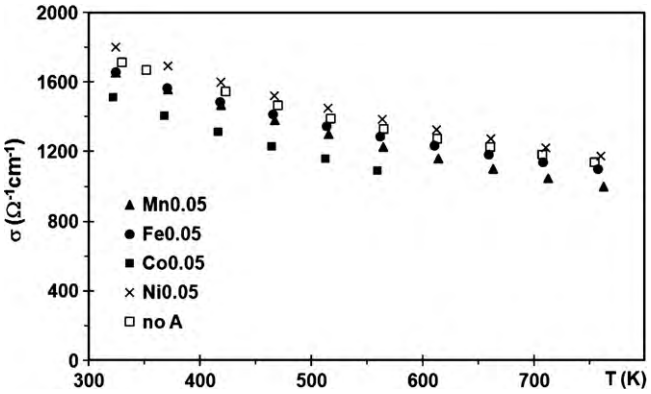

Fig. 5. Electrical conductivity of $A_{0.05}Mo_3Sb_{5.4}Te_{1.6}$ (A = Mn, Fe, Co, Ni) and $Mo_3Sb_{5.4}Te_{1.6}$.

(S) between $+55\,\mu V\,K^{-1}$ and $+65\,\mu V\,K^{-1}$ around 320 K (Fig. 6). With an experimental error of $1\,\mu V\,K^{-1}$, the differences are significant. S increases in all cases with increasing temperature, typical for samples with constant charge carrier concentration, reaching a maximum of $+170\,\mu V\,K^{-1}$ at 950 K in case of $Fe_{0.05}Mo_3Sb_{5.4}Te_{1.6}$. The samples with the highest electrical conductivity, $Ni_{0.05}Mo_3Sb_{5.4}Te_{1.6}$ and $Mo_3Sb_{5.4}Te_{1.6}$, have the lowest

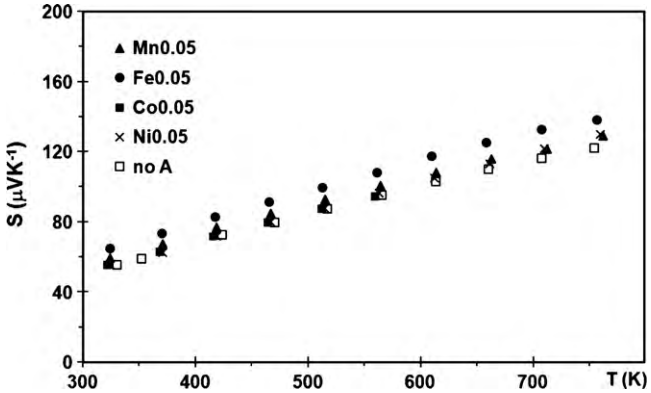

Fig. 6. Seebeck coefficient of $A_{0.05}Mo_3Sb_{5.4}Te_{1.6}$ (A = Mn, Fe, Co, Ni) and $Mo_3Sb_{5.4}Te_{1.6}$.

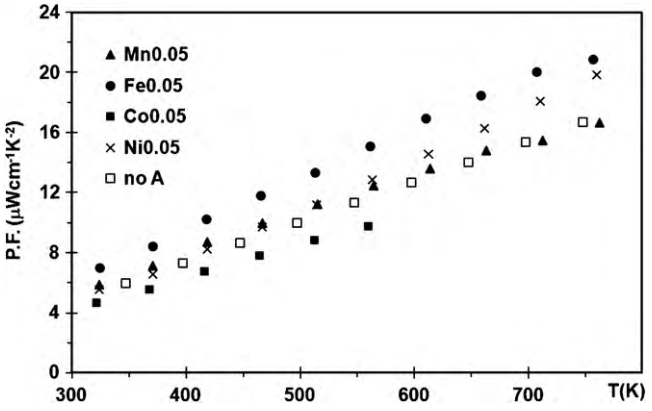

Fig. 7. Power factor (P.F.) of $A_{0.05}Mo_3Sb_{5.4}Te_{1.6}$ (A = Mn, Fe, Co, Ni) and $Mo_3Sb_{5.4}Te_{1.6}$.

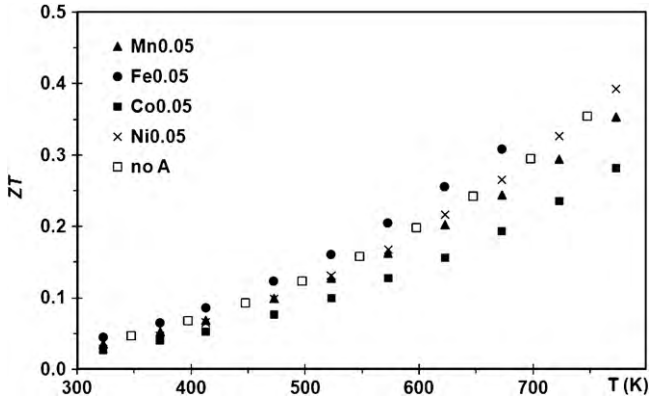

Fig. 9. Thermoelectric figure-of-merit *ZT* of $A_{0.05}Mo_3Sb_{5.4}Te_{1.6}$ (A = Mn, Fe, Co, Ni) and $Mo_3Sb_{5.4}Te_{1.6}$.

Seebeck coefficient values. $Fe_{0.05}Mo_3Sb_{5.4}Te_{1.6}$ has the highest Seebeck coefficient, indicating that its derivative of the DOS at E_F is large—see Eq. (2) [34,35].

$$S = \frac{1}{\mathrm{DOS}(E_F)}\left(\frac{\partial[\mathrm{DOS}(E)}{\partial E}\right)_{E-E_F} \quad (2)$$

The power factor (P.F. = $S^2\sigma$) reflects the combined impact of Seebeck coefficient and electrical conductivity onto *ZT* (sometimes P.F. is alternatively defined as the product of S^2, σ and *T*). Because of its highest Seebeck coefficient and intermediate electrical conductivity, $Fe_{0.05}Mo_3Sb_{5.4}Te_{1.6}$ exhibits the highest power factor in the whole temperature range measured (Fig. 7), with P.F.(320 K) = 7.0 μW cm^{-1} K^{-2} and P.F.(950 K) = 27.6 μW cm^{-1} K^{-2}, respectively. $Ni_{0.05}Mo_3Sb_{5.4}Te_{1.6}$, $Mn_{0.05}Mo_3Sb_{5.4}Te_{1.6}$ and $Mo_3Sb_{5.4}Te_{1.6}$ have very comparable power factor values below 570 K. With rising temperature, P.F. of $Ni_{0.05}Mo_3Sb_{5.4}Te_{1.6}$ increases faster. For example, $Ni_{0.05}Mo_3Sb_{5.4}Te_{1.6}$ has a P.F.(770 K) = 20.2 μW cm^{-1} K^{-2}, $Mn_{0.05}Mo_3Sb_{5.4}Te_{1.6}$ a P.F.(770 K) = 17.9 μW cm^{-1} K^{-2} and $Mo_3Sb_{5.4}Te_{1.6}$ a P.F.(800 K) = 18.1 μW cm^{-1} K^{-2}. $Co_{0.05}Mo_3Sb_{5.4}Te_{1.6}$ has the lowest power factor within this series of samples mostly due to its lowest electrical conductivity. All the power factor values mentioned above are significantly higher than the power factor of $Yb_{14}MnSb_{11}$, one of the leading *p*-type thermoelectric materials, which exhibits its maximum P.F. = 6 μW cm^{-1} K^{-2} at 1200 K [9].

Last, the thermal conductivity, being the sum of the lattice contribution (κ_L) and the contribution from the charge carriers (κ_{el}), is generally decreasing with increasing temperature (Fig. 8), as κ_L decreases because of the increasing lattice vibration and κ_{el} as seen in the electrical conductivity measurements. All quaternary antimonide–tellurides $A_{0.05}Mo_3Sb_{5.4}Te_{1.6}$ (A = Mn, Co, Fe, Ni) have higher thermal conductivity values than $Mo_3Sb_{5.4}Te_{1.6}$, with κ between 5.2 W m^{-1} K^{-1} ($Fe_{0.05}Mo_3Sb_{5.4}Te_{1.6}$) and 5.6 W m^{-1} K^{-1} ($Co_{0.05}Mo_3Sb_{5.4}Te_{1.6}$) at 320 K and 2.1 W m^{-1} K^{-1} ($Fe_{0.05}Mo_3Sb_{5.4}Te_{1.6}$) to 2.7 W m^{-1} K^{-1} ($Co_{0.05}Mo_3Sb_{5.4}Te_{1.6}$) at 670 K, compared to 4.5 W m^{-1} K^{-1} for $Mo_3Sb_{5.4}Te_{1.6}$ at 320 K. The observation of a 13–20% lower κ of $Mo_3Sb_{5.4}Te_{1.6}$ is consistent with the low temperature data presented earlier [13], and compares well with the data on $Mo_3Sb_{5.4}Te_{1.6}$ presented by Gascoin et al. [15]. That difference must come from the lattice contributions, because the electrical conductivity values and thus the electronic contributions are comparable; in fact, $Mo_3Sb_{5.4}Te_{1.6}$ exhibits the second highest electrical conductivity of the materials investigated here. The fact that the thermal conductivity increases upon intercalation of the *3d* transition metal atoms indicates that the additional atoms act as space fillers rather than rattlers, decreasing the porosity of the material.

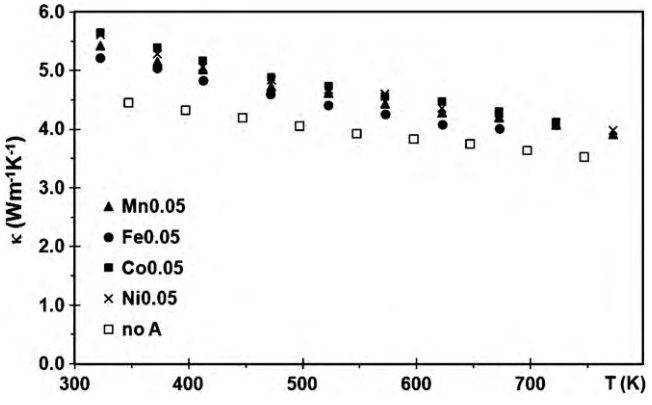

Fig. 8. Thermal conductivity of $A_{0.05}Mo_3Sb_{5.4}Te_{1.6}$ (A = Mn, Fe, Co, Ni) and $Mo_3Sb_{5.4}Te_{1.6}$.

Compared with the thermal conductivity of $Yb_{14}MnSb_{11}$, the high thermal conductivity of these antimonide–tellurides is their main disadvantage. The very low thermal conductivity of $Yb_{14}MnSb_{11}$ (e.g. 0.8 W m^{-1} K^{-1} at 300 K) results in high *ZT* values in spite of its relatively small power factor [9].

Because the thermal conductivity was measured at different temperatures than Seebeck coefficient and electrical conductivity, linear fits of the power factor ($S^2\sigma$) combined with the measured thermal conductivity (κ) were used to determine *ZT*. The uncertainty of the ZT values is estimated to be 5–7%. The thus calculated *ZT* curves increase rapidly with increasing temperature (Fig. 9) because of the simultaneous increase of P.F. (and *T*) and decrease of κ. $Fe_{0.05}Mo_3Sb_{5.4}Te_{1.6}$ presents the largest *ZT* values here, which may be extrapolated to reach *ZT* = 0.85 at 1023 K like $Yb_{14}MnSb_{11}$ [9]. $Co_{0.05}Mo_3Sb_{5.4}Te_{1.6}$ has the lowest *ZT*, and $Ni_{0.05}Mo_3Sb_{5.4}Te_{1.6}$, $Mo_3Sb_{5.4}Te_{1.6}$ and $MnMo_3Sb_{5.4}Te_{1.6}$ exhibit very comparable *ZT* values in the whole temperature range, varying from 0.03 at 322 K to 0.39 at 772 K.

3.5. Thermal analysis

DSC measurements for $Ni_{0.05}Mo_3Sb_{5.4}Te_{1.6}$ and Mo_3Sb_7 were carried out at the University of Waterloo. The downtrend of the $Ni_{0.05}Mo_3Sb_{5.4}Te_{1.6}$ curve below 1100 K is caused by an overcorrection of the baseline (Fig. 10). The decomposition of Mo_3Sb_7 into the elements Mo and Sb occurs at 1263 K, and the decomposition of $Ni_{0.05}Mo_3Sb_{5.4}Te_{1.6}$ peaks at 1326 K. Both of these two temperatures are much higher than the earlier reported decomposition temperature of Mo_3Sb_7 of 1073 K [36]. X-ray diagrams obtained after these experiments revealed the existence of Mo, Sb, $Ni_xMo_3(Sb,Te)_7$ and $MoTe_2$. Apparently $Ni_{0.05}Mo_3Sb_{5.4}Te_{1.6}$ can

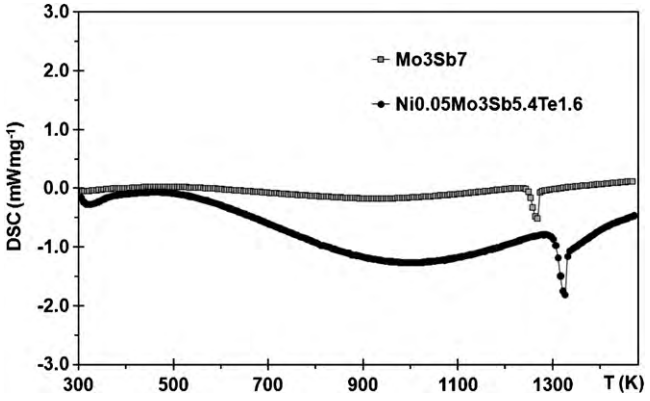

Fig. 10. DSC curves of $Ni_{0.05}Mo_3Sb_{5.4}Te_{1.6}$ and Mo_3Sb_7.

endure higher temperatures than Mo_3Sb_7, likely of a consequence of the additional filled bonding states because of the larger valence electron concentration [31].

4. Conclusions

The high temperature thermoelectric properties of $A_{0.05}Mo_3Sb_{5.4}Te_{1.6}$ (A = Mn, Fe, Co and Ni) and $Mo_3Sb_{5.4}Te_{1.6}$ were examined and compared in this paper. Compared to other thermoelectrics, these samples exhibit high power factor values, but also rather high thermal conductivity. Adding Fe and Ni can increase the power factor of $A_{0.05}Mo_3Sb_{5.4}Te_{1.6}$ over that of $Mo_3Sb_{5.4}Te_{1.6}$; however, the thermal conductivity is increased in all cases with addition of transition metal atoms.

An enhancement of the thermoelectric *ZT* value, compared to $Mo_3Sb_{5.4}Te_{1.6}$, was achieved upon addition of Fe and Ni atoms. The best compound $Fe_{0.05}Mo_3Sb_{5.4}Te_{1.6}$ obtains $ZT = 0.31$ at 673 K. This value is higher than that of $Ni_{0.05}Mo_3Sb_{5.4}Te_{1.6}$ ($ZT = 0.27$ at 673 K), but lower than the value of $Ni_{0.06}Mo_3Sb_{5.4}Te_{1.6}$ ($ZT = 0.34$ at 673 K) that we reported in 2009 [20]. The latter reaches $ZT > 0.9$ above 1000 K. We will attempt to lower the thermal conductivity during ongoing research, for example via different consolidation techniques after ball-milling and via using nanocomposites.

Acknowledgments

Financial support from NSERC and Canada Research Chair program (CRC for H.K.) is appreciated. We acknowledge the partial support from the Donors of the American Chemical Society Petroleum Research Fund. We further appreciate the support from a DOE/EPSCoR Implementation Grant (#DE-FG02-04ER-46139) and from the SC EPSCoR Office, Clemson University and McMaster University for the work highlighted in this paper.

References

[1] T.M. Tritt, Science 283 (1999) 804–805.
[2] J. Yang, T. Caillat, Mater. Res. Bull. 31 (2006) 224–229.
[3] D.M. Rowe, CRC Handbook of Thermoelectrics, CRC Press, Boca Raton, FL, 1995.
[4] T.M. Tritt, Science 272 (1995) 1276–1277.
[5] F.J. DiSalvo, Science 285 (1999) 703–706.
[6] G.J. Snyder, E.S. Toberer, Nat. Mater. 7 (2008) 105–114.
[7] E.S. Toberer, A.F. May, G.J. Snyder, Chem. Mater. 22 (2010) 624–634.
[8] C.B. Vining, W. Laskow, J.O. Hanson, R.R. Van der Beck, P.D. Gorsuch, J. Appl. Phys. 69 (1991) 4333–4340.
[9] S.R. Brown, S.M. Kauzlarich, F. Gascoin, G.J. Snyder, Chem. Mater. 18 (2006) 1873–1877.
[10] K.F. Hsu, S. Loo, F. Guo, W. Chen, J.S. Dyck, C. Uher, T. Hogan, E.K. Polychroniadis, M.G. Kanatzidis, Science 303 (2004) 818–821.
[11] E. Dashjav, A. Szczepenowska, H. Kleinke, J. Mater. Chem. 12 (2002) 345–349.
[12] N. Soheilnia, E. Dashjav, H. Kleinke, Can. J. Chem. 81 (2003) 1157–1163.
[13] H. Zhang, J. He, B. Zhang, Z. Su, T.M. Tritt, N. Soheilnia, H. Kleinke, J. Electron Mater. 36 (2007) 727–731.
[14] H. Xu, N. Soheilnia, H. Zhang, P.N. Alboni, T.M. Tritt, H. Kleinke, Mater. Res. Soc. Symp. Proc. 1044 (2008) 459–467.
[15] F. Gascoin, J. Rasmussen, G.J. Snyder, J. Alloys Compd. 427 (2007) 324–329.
[16] C. Candolfi, B. Lenoir, A. Dauscher, E. Guilmeau, J. Hejtmánek, J. Tobola, B. Wiendlocha, S. Kaprzyk, Phys. Rev. B 79 (2009), 035114/035111–035114/035116.
[17] C. Candolfi, B. Lenoir, A. Dauscher, J. Hejtmánek, J. Tobola, Phys. Rev. B 79 (2009), 235108/235101–235108/235112.
[18] C. Candolfi, B. Lenoir, J. Leszczynski, A. Dauscher, E. Guilmeau, J. Appl. Phys. 105 (2009), 083701/083701–083701/083704.
[19] C. Candolfi, B. Lenoir, J. Leszczynski, A. Dauscher, J. Tobola, S.J. Clarke, R.I. Smith, Inorg. Chem. 48 (2009) 5216–5323.
[20] H. Xu, K.M. Kleinke, T. Holgate, H. Zhang, Z. Su, T.M. Tritt, H. Kleinke, J. Appl. Phys. 105 (2009), 053703/053701–053703/053705.
[21] M. Zelinska, A. Assoud, C. Graf, H. Kleinke, Inorg. Chem. 49 (2010) 1090–1093.
[22] O.K. Andersen, Phys. Rev. B 12 (1975) 3060–3083.
[23] H.L. Skriver, The LMTO Method, Springer, Berlin, Germany, 1984.
[24] L. Hedin, B.I. Lundqvist, J. Phys. C 4 (1971) 2064–2083.
[25] W.R.L. Lambrecht, O.K. Andersen, Phys. Rev. B 34 (1986) 2439–2449.
[26] P.E. Blöchl, O. Jepsen, O.K. Andersen, Phys. Rev. B 49 (1994) 16223–16233.
[27] A.L. Pope, R.T. Littleton IV, T.M. Tritt, Rev. Sci. Instrum. 72 (2001) 3129–3131.
[28] F. Jellinek, H. Hahn, Naturwiss 49 (1962) 103.
[29] R. Ceolin, N. Rodier, P. Khodadad, J. Less-Comm. Met. 53 (1977) 137–140.
[30] C. Candolfi, B. Lenoir, A. Dauscher, J. Tobola, S.J. Clarke, R.I. Smith, Chem. Mater. 20 (2008) 6556–6561.
[31] J. Xu, H. Kleinke, J. Comput. Chem. 29 (2008) 2134–2143.
[32] P. Stadelmann, JEMS—Java Electron Microscopy Software, Version 2.0819W2005, EPFL, Switzerland, 2001.
[33] H. Kleinke, Chem. Mater. 22 (2010) 604–611.
[34] N.F. Mott, H. Jones, The Theory of the Properties of Metals and Alloys, Dover Publications, New York, NY, 1958.
[35] G.D. Mahan, J.O. Sofo, Proc. Natl. Acad. Sci. U.S.A. 93 (1996) 7436–7439.
[36] P. Jensen, A. Kjekshus, T. Skansen, Acta Chem. Scand. 20 (1966) 403–416.